

Article

Using UAS-Aided Photogrammetry to Monitor and Quantify the Geomorphic Effects of Extreme Weather Events in Tectonically Active Mass Waste-Prone Areas: The Case of Mediane Ianos

Evelina Kotsi ¹, Emmanuel Vassilakis ^{1,*}, Michalis Diakakis ², Spyridon Mavroulis ², Aliko Konsolaki ¹, Christos Filis ², Stylianos Lozios ² and Efthymis Lekkas ²

¹ Remote Sensing Laboratory, Department of Geology and Geoenvironment, School of Sciences, National and Kapodistrian University of Athens, Panepistimiopolis Zografou, 15784 Athens, Greece

² Section of Dynamic Tectonic Applied Geology, Department of Geology and Geoenvironment, School of Sciences, National and Kapodistrian University of Athens, Panepistimiopolis Zografou, 15784 Athens, Greece

* Correspondence: evasilak@geol.uoa.gr; Tel.: +30-210-727-4400

Abstract: Extreme weather events can trigger various hydrogeomorphic phenomena and processes including slope failures. These shallow instabilities are difficult to monitor and measure due to the spatial and temporal scales in which they occur. New technologies such as unmanned aerial systems (UAS), photogrammetry and the structure-from-motion (SfM) technique have recently demonstrated capabilities useful in performing accurate terrain observations that have the potential to provide insights into these geomorphic processes. This study explores the use of UAS-aided photogrammetry and change detection, using specialized techniques such as the digital elevation model (DEM) of differences (DoD) and cloud-to-cloud distance (C2C) to monitor and quantify geomorphic changes before and after an extreme mediane event in Myrtos, a highly visited touristic site on Cephalonia Island, Greece. The application demonstrates that the combination of UAS with photogrammetry allows accurate delineation of instabilities, volumetric estimates of morphometric changes, insights into erosion and deposition processes and the delineation of higher-risk areas in a rapid, safe and practical way. Overall, the study illustrates that the combination of tools facilitates continuous monitoring and provides key insights into geomorphic processes that are otherwise difficult to observe. Through this deeper understanding, this approach can be a stepping stone to risk management of this type of highly-visited sites, which in turn is a key ingredient to sustainable development in high-risk areas.

Keywords: extreme events; unmanned aerial vehicles; UAV; photogrammetry; DEM of differences; landslides; debris flows; sustainable development; medianes; geomorphic processes



Citation: Kotsi, E.; Vassilakis, E.; Diakakis, M.; Mavroulis, S.; Konsolaki, A.; Filis, C.; Lozios, S.; Lekkas, E. Using UAS-Aided Photogrammetry to Monitor and Quantify the Geomorphic Effects of Extreme Weather Events in Tectonically Active Mass Waste-Prone Areas: The Case of Mediane Ianos. *Appl. Sci.* **2023**, *13*, 812. <https://doi.org/10.3390/app13020812>

Academic Editor: José A. Peláez

Received: 25 November 2022

Revised: 29 December 2022

Accepted: 3 January 2023

Published: 6 January 2023



Copyright: © 2023 by the authors. Licensee MDPI, Basel, Switzerland. This article is an open access article distributed under the terms and conditions of the Creative Commons Attribution (CC BY) license (<https://creativecommons.org/licenses/by/4.0/>).

1. Introduction

Slope failures and mass movement phenomena are important hazards around the globe [1,2]. Especially in tectonically active areas, steep slopes are characterized by deformed geological formations and sharp relief [3,4]. Landslides and other such instabilities often cause significant impacts on infrastructure [5,6], disruption of socio-economic activities, and numerous fatalities [7–10]. Extreme weather events are one of the most common triggers of these failures [11–14]. Especially around the Mediterranean region, shallow landslides and debris flows triggered by extreme climatic events have led to catastrophic impacts in the past [15–20].

Given that the region is one of the most sensitive to climate change across the globe [21–23] and that intense climatic events can potentially become more frequent in the future [24–27], the increase in associated phenomena and hazards (i.e., floods, landslides and debris flows) can be a threat as well.

The Mediterranean region is also dominated by high-value land uses, rich with important socioeconomic activity, including trade, tourism, transportation and others, especially along the coast [28,29], making it highly vulnerable to the occurrence of natural hazards [30–32].

Recent research has shown the competence of new technologies such as unmanned aerial systems (hereafter referred to as UASs) processed by structure-from-motion (SfM) photogrammetry and multi-view stereo (MVS) in mapping and measuring geomorphological features to acquire high-resolution topography data [33,34]. Such approaches used in certain recent studies have illustrated that UASs can be a powerful tool for producing high-resolution terrain modeling, illustrating accuracy and shedding light into the dynamics of geomorphological processes [35,36]. Photogrammetric processes, along with geomorphic analysis methodologies, have seen a rise in application in multiple fields of geosciences and surveying [37,38]. Some of these applications focus on fluvial geomorphology [39], channel dynamics [40,41], hydro-geomorphological processes [42], landslides, debris flows [43,44], detailed topography [33], classification of fluvial geomorphological features and other geomorphic phenomena [38]. Most of these studies capitalize on photogrammetry's capacity for high-resolution mapping together with UAS' capabilities for rapid mapping [41].

The complexity of mass wasting processes and the threat of climate change, together with the high exposure of infrastructure and high hazard levels in the Mediterranean coasts and their importance in local socioeconomic activities, highlight the need for an in-depth understanding of the extent and characteristics of slope failures and mass movement phenomena caused by extreme weather events. Monitoring these effects is important for minimizing disruptions from such events and is the basis for sustainable development. A deep understanding of the risks and the natural processes that create them, together with micro-zonation of high-value sites, can be a valuable tool so that these areas are able to retain their use, continue their socioeconomic activities with minimum disruption and at the same time keep high standards of safety [45,46].

In this context, the objective of the present study is to explore the capabilities of UASs in conjunction with photogrammetry in investigating mass movement phenomena along slopes through measurements of morphometric changes, shedding light into erosion/deposition processes, and delineate areas unsuitable for development. To this aim, this study explores the geomorphological impacts of Medicane Ianos (an extreme event that occurred in September 2020) in the area of the Ionian Islands in Greece, and specifically on the famous Myrtos beach, a highly touristic, tectonically active area, with a rich history of landslides [47–50], investigating and discussing the advantages and disadvantages of the application.

2. Study Area

2.1. Geological Setting

Cephalonia is located in the Ionian Islands group, a group of seven islands in the westernmost part of Greece. From the geotectonic viewpoint, Cephalonia is situated at the northwestern part of the Hellenic Arc (Figure 1), in a tectonically complex and seismically active area, where strike-slip movement prevails along the Cephalonia Transform Fault Zone (CTFZ) [51–53], generating the strong and intense seismic activity observed in the region [54].

The geological structure of Cephalonia includes alpine formations and post-alpine deposits [55–61]. The alpine formations are classified into two geotectonic units of the External Hellenides: (a) the Ionian and (b) the Paxi unit. The Ionian unit is located in the eastern part of the island and includes Triassic evaporites, Jurassic–Cretaceous limestones and the Upper Eocene–Lower Miocene flysch at the top of the sequence [55,56]. The Paxi unit covers the rest of the island and comprises mainly carbonate rocks from the Triassic to Middle Miocene and a Middle Miocene–Early Pliocene clay-clastic flyschoid, which includes marls, clays and limestones [55,56]. The post-alpine deposits lay unconformably over the alpine formations. They occur mainly in the western, southern and southeastern parts of

Cephalonia. They mainly include a Pliocene–Calabrian sequence and Pleistocene–Holocene formations [55,56]. The Pliocene–Calabrian sequence constitutes a marine sequence mainly observed in the eastern and western part of the Paliki peninsula and in the largest part of the Argostoli peninsula. The Middle–Upper Pleistocene–Holocene formations comprise continental deposits and are classified into Middle Pleistocene marine calcarenites, Pleistocene interglacial deposits, Pleistocene scree and Holocene deposits [55,56].

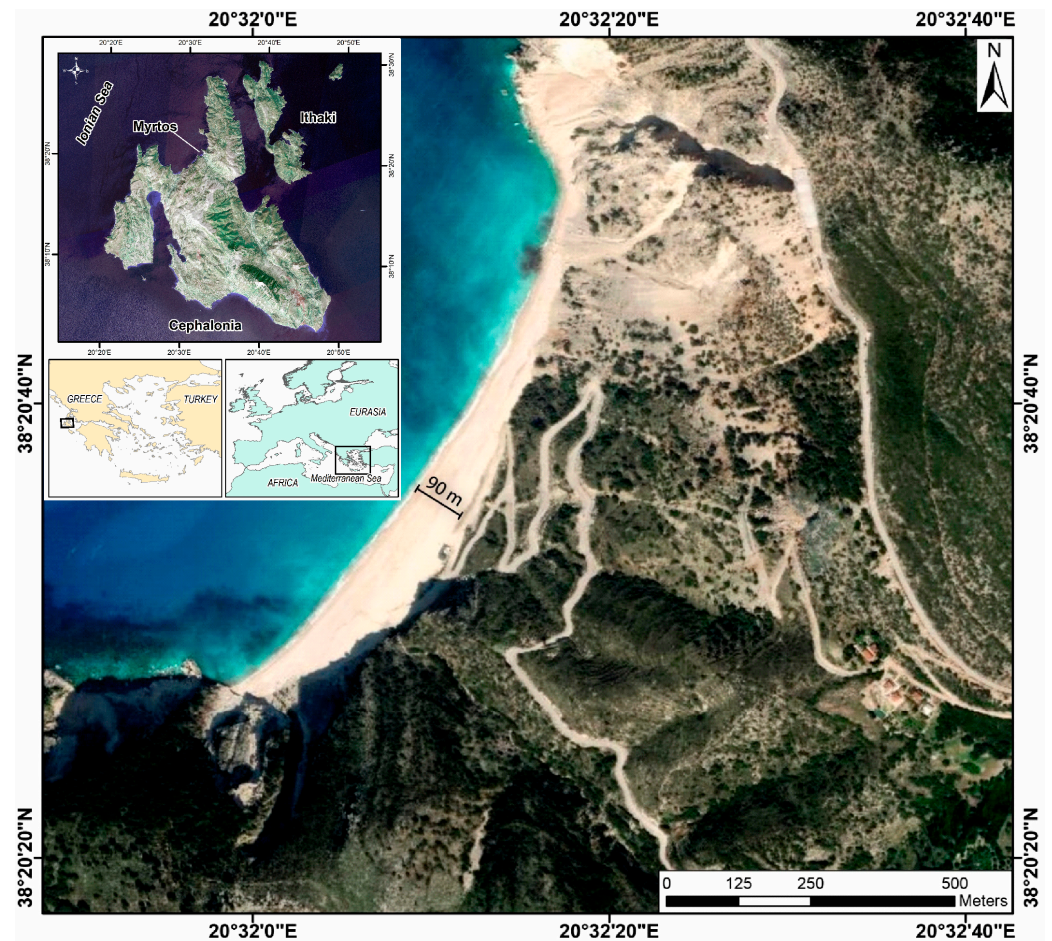


Figure 1. Location map of Myrtos beach. The insets show the study site at different scales (projected coordinate system GGRS'87, EPSG:2100).

As far as the neotectonic structure of the island is concerned, Cephalonia is composed of large fault blocks, which are distinguished from each other by major fault zones and faults [47,55,62]. The fault block of the Erissos peninsula is located in the northern part of the island, which is almost exclusively composed of Triassic–Middle Miocene limestones of the Paxi unit. On its south boundary lies the Agia Efimia oblique-slip reverse fault, which is observed along the southern slopes of Kalon Mt and places the Erissos fault block on the northeastern part of the Aenos Mt fault block. The Aenos and eastern Cephalonia fault block is the largest on the island. On its northern boundary lies the oblique-slip reverse Agia Efimia fault, on the west the Kontogourata–Agonas oblique-slip reverse fault, which places the northwestern part of the Aenos fault on the Paliki peninsula. To the south, it is bordered by the Aenos Mt fault zone, along the faults of which extensive amounts of scree have been formed. The Aenos fault block is mainly composed of Paxi formations, particularly of Triassic–Middle Miocene limestones in its western and central parts, while eastern Cephalonia is composed of Ionian formations, including Triassic evaporites, Jurassic–Cretaceous limestones and Upper Eocene–Lower Miocene flysch [47,55]. The Paliki and

Argostoli peninsulas in western and southern Cephalonia complement the puzzle of the neotectonic faults of the island.

In terms of climate, the Ionian Islands group stretches roughly from the north to the south of the Ionian Sea, along the coast of western continental Greece, positioned on the boundary between the Western and the Eastern Mediterranean. The islands are situated in an area through which most of the western weather systems enter the Eastern Mediterranean region. The Ionian Islands are exposed to synoptic systems from the Northwest (the Balearic Sea, Gulf of Lions, Gulf of Genoa, and the Adriatic Sea) [63] and Southwest areas (Gulfs of Sidra and Gabes) [64,65], as well as the Ionian Sea itself. These systems are intensified by the warm waters of the Mediterranean before reaching the Ionian islands, giving them a very unique position when it comes to precipitation [66] and other extreme events [67]. In multiple instances in the last decade, the area has been hit by numerous systems, including four medicanes [65,68], causing various hydro-geomorphic phenomena including flooding and slope instabilities. Climatic changes in the future in the broader area can potentially increase these adverse effects of medicanes [24,26].

2.2. Study Site

In the transition zone between the Erissos peninsula and the northeastern part of the Aenos fault block (Figure 2), the Pylaros valley was formed in a NW-SE direction. It is mainly composed of the Middle Miocene–Upper Miocene clay-clastic series of the Paxi unit and secondarily by Holocene alluvial deposits. The coastal area of Myrtos is located at the northwestern end of the Pylaros valley. The morphology of the area is characterized by very high slope values, locally exceeding 50°. This rugged morphology is the result of intense tectonic uplift. Indicative of the tectonic processes prevailing in this area is the uplift induced by the August 1953 seismic sequence, which ranges from 40 to 70 cm [69]. The same was not the case at the southeastern end of the Pylaros valley, where the uplift ranges from 15 to 25 cm [69], giving an asymmetric character.

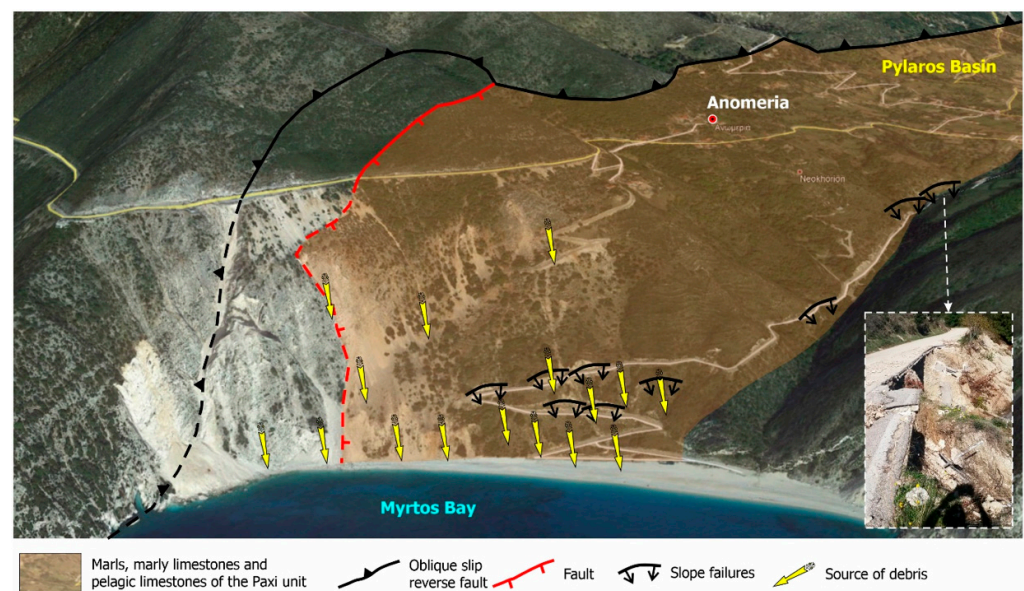


Figure 2. The morphological, geological, tectonic, and geotechnical context of the generation of destructive slope failures on the steep slopes of the Myrtos coastal area, based on geological field surveys in the area.

The steep slopes, combined with the reduced geotechnical characteristics of clastic formations and the overlying scree mantle, create favorable conditions for the generation of large-scale failures along the slopes of the Myrtos coastal area (Figures 2 and 3). These failures are usually generated in the form of slides and rockfalls in the case of earthquakes [47,49,50], and debris and mud flows in the case of heavy rainfall [70]. Furthermore,

the dip of the beds is similar to the dip of slopes, which creates another ideal situation for triggering slope failures, especially during strong earthquake ground motion. The combined action of the factors above, along with the groundwater level and the presence of small springs along the slopes and human interventions comprising the construction of a road leading to Myrtos beach (Figures 2 and 3), intensify the instability of the coastal formations and slopes.

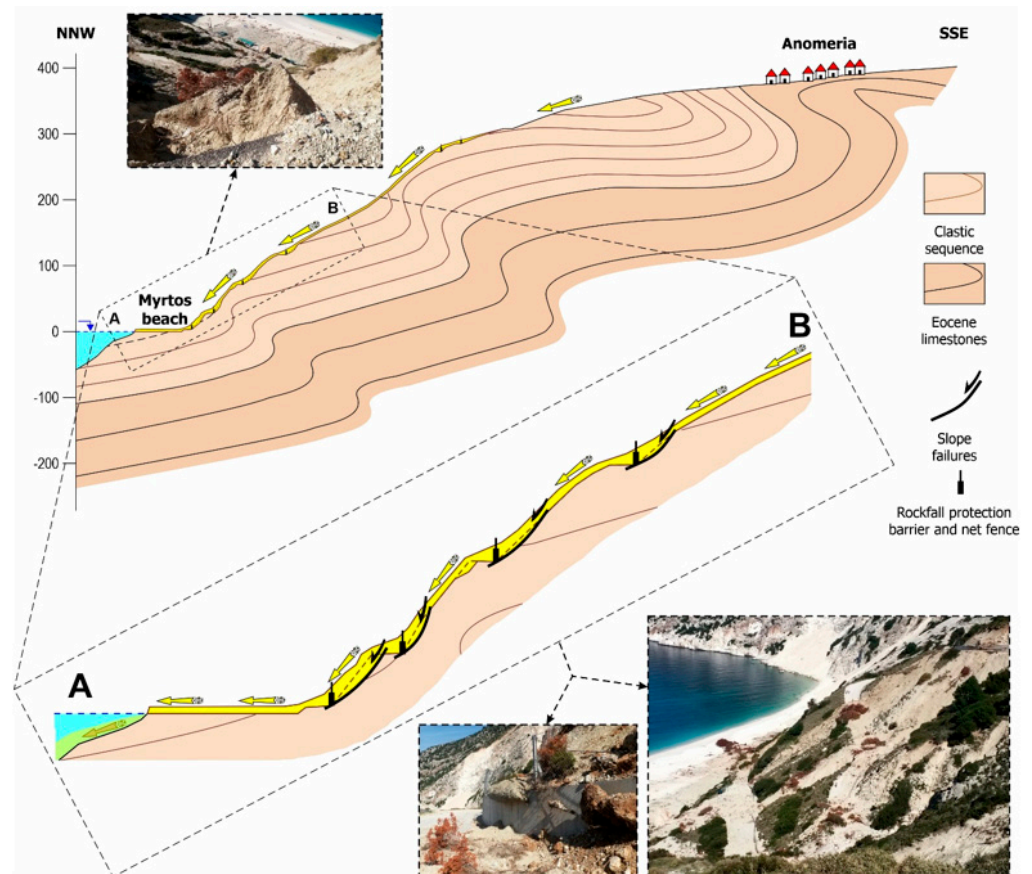


Figure 3. The geological, tectonic, and geotechnical setting of the steep slopes of the Myrtos coastal area, based on geological field surveys.

Taking into account the results of Mavroulis et al. [50] regarding the landslide susceptibility of Cephalonia, the Myrtos coastal area is characterized as an area of critically high susceptibility. As shown by the earthquake-triggered landslides records of Cephalonia from 1636 to 2014 presented in the aforementioned study, landslides were triggered in the Myrtos coastal area by the 1953, 1983, and 2014 earthquakes. Based on modern data on the August 1953 earthquake sequence, a boulder was detached from a slope in the Myrtos coastal area and ended up in the adjacent bay, causing water turbidity [49,50]. The 17 January 1983 $M_s = 7.0$ earthquake triggered slope failures at the Charakas site located on the northern slope of Myrtos bay [49,50,71]. Landslides occurred along a sub-vertical artificial road cut, resulting in accumulation of limestone boulders and debris on the adjacent road and temporary traffic disruption. Downstream of the Charakas road, rockfalls were also triggered, resulting in water turbidity once again. The most recent earthquake-triggered landslides in Myrtos are attributed to the early 2014 earthquakes on January 26 ($M = 6.1$) and February 3 ($M = 5.9$) [48]. Two limestone boulders were detached from the slope over the beach, and rolled down the slope, stopping on the beach at a distance of about 100 m from the shoreline.

2.3. Medicane Ianos Event

In mid-September 2020, a depression that formed near the Libyan coast in the north-west of the Gulf of Sidra developed into a Mediterranean cyclone (medicane), which moved north towards the Ionian Sea and SW Greece. The medicane, named “Ianos”, hit land on 18 September 2020 in Greece, affecting a large part of the country from Crete (southern Greece) to Thessaly (central Greece), causing severe damage to property and infrastructure induced by intense precipitation, flash flooding, strong winds and wave action. It also caused human casualties [70].

The system affected the central Ionian Islands (Lefkada, Cephalonia, Ithaki, and Zakynthos), the northwestern Peloponnese, as well as central Thessaly and other areas of central Greece, causing widespread flooding and associated disasters [68,70,72,73]. Then, heading towards southern Greece, it weakened until its final completion on 21 September.

During its destructive route, Ianos exhibited strong winds, heavy rainfall, and thunderstorms. Based on the recordings of the EAA weather stations, the maximum rainfall in Western Greece was recorded in the Ionian Islands (reaching an accumulated value of 769 mm and 250 mm on Cephalonia and Zakynthos Islands, respectively, in 48 h [68]). Its impacts, apart from the four fatalities, extended to coastal and inland rural and urban areas and were observed on vegetation, properties, vehicles, and boats. It also impacted the infrastructure, including parts of the road network and health facilities and structures, railway lines, power supply network, drinking water, and telecommunications, as well as coastal infrastructure, including port facilities and coastal roads, across the island (Figure 4) [70].

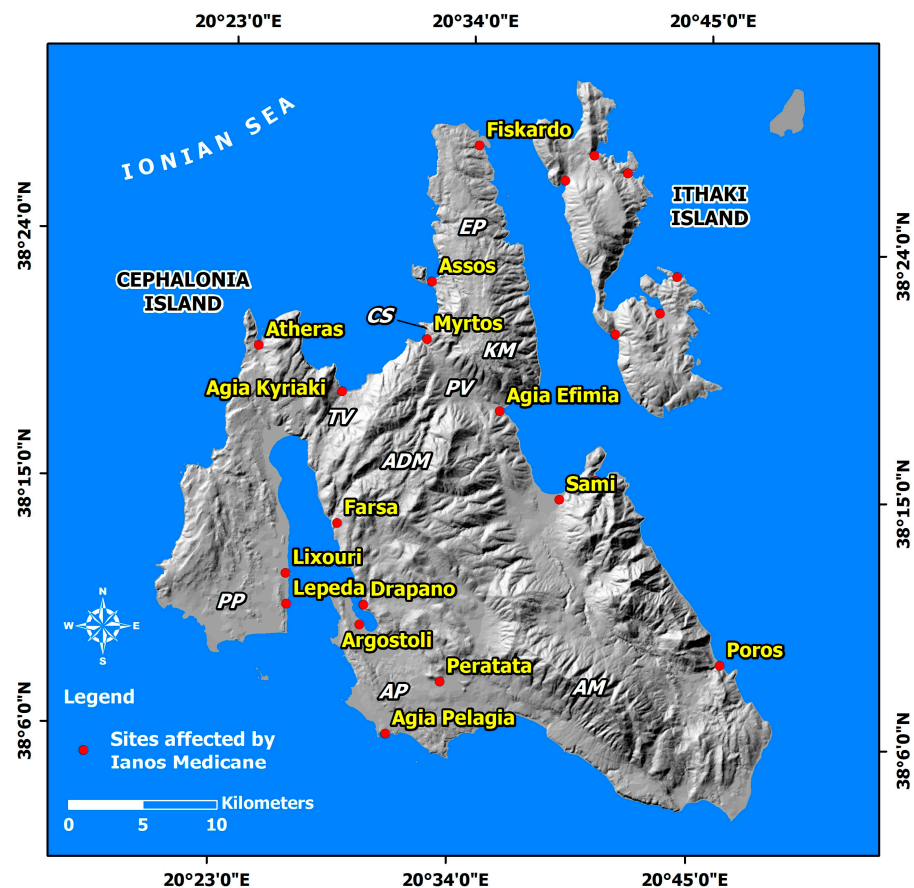


Figure 4. Spatial distribution of sites affected by Medicane Ianos in Cephalonia Island. EP: Erissos Peninsula; CS: Charakas site; KM: Kalon Mt; PV: Pylaros valley; TV: Thinia Valley; ADM: Agia Dynati Mt; AM: Aenos Mt; AP: Argostoli peninsula. The study area of Myrtos is located at the western end of Pylaros valley corresponding to the transition zone from the Erissos peninsula to the mountainous central Cephalonia.

The most striking effects were reported in Assos, Agia Efimia, and Myrtos coastal areas [70]. In Assos, material from debris and mud flows covered parts of the road network and rushed into public and private areas, causing traffic disruption, vehicle entrapment in parts of the road network, and blocking houses for several days until debris removal (Figure 5). The debris flooded the coastal front and partially covered the road, the harbor, and adjacent beaches, altering the landscape (Figure 5). Furthermore, vessels in the port suffered damage not only from the strong sea waves but also from debris from flows and floods (Figure 5).

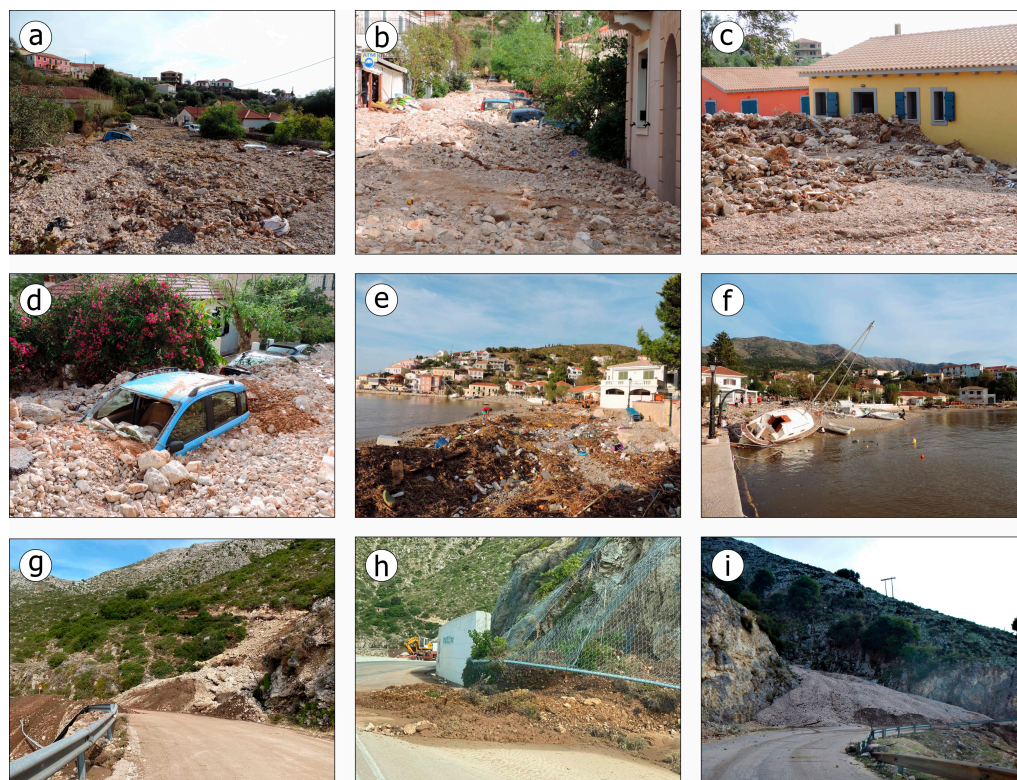


Figure 5. Typical views of the impact of Mediane Ianos on Cephalonia Island: (a–d) debris inundated public and private areas of Assos village causing minor non-structural damage to buildings and blockage of ground floor entrances. (e, f) The port of Assos village was also affected by the generated debris flows. Debris flooded the coastal road, part of the port, and the adjacent beaches, resulting in morphological changes. (f–i) Debris flows were also triggered in several sites in the Agia Efimia area, resulting in temporary traffic disruption due to accumulation of debris on adjacent parts of the road network. Assos is located in the western part of the Erissos peninsula, while Agia Efimia is located in the eastern part of the transition zone from the Erissos peninsula in the north to the Aenos Mt fault block to the south.

In Agia Efimia, vehicles parked along the road network were swept away by flood waters and overturned, resulting in severe damage and in some cases complete destruction. The flood waters carried away objects of various dimensions from the exterior and interior of residential buildings, which accumulated in the coastal zone, creating additional problems in the operation of the networks and the implementation of restoration operations.

2.4. Slope Failures in Myrtos Due to the Mediane Ianos

Debris and mud flows were triggered by the heavy rainfall that struck the Myrtos coastal area during the passing of Mediane Ianos over Cephalonia. The mobilized material was initially retained by the existing slope protection works constructed after the early 2014 earthquakes on the island (Figure 6). These works constructed along the road leading

to Myrtos beach included rockfall protection barriers or catchment fences with I-beam posts spaced at certain intervals, with a wire rope support system running from post to post and special friction devices placed on the top support ropes. Wire rope nets were attached to the support system and backed with a wire mesh for retaining small stones and rocks. However, with the continuation of the rainfall and the amplification of the generated debris and mud flows during Medicane Ianos, the space behind the barriers and fences was quickly filled (Figure 6a) so that in several sites the ongoing material flows passed over them (Figure 6b) and they were effectively disabled (Figure 6c). As a result, many sections of the road leading to the beach were covered with debris and mud, and traffic was temporarily disrupted (Figure 6d) until the removal of the debris and the completion of the recovery actions. In addition, the material that was finally deposited at the base of the slope caused severe damage to visitor facilities, including a refreshment center, WC, a parking site, and a sunlounge site (Figure 6d–g).

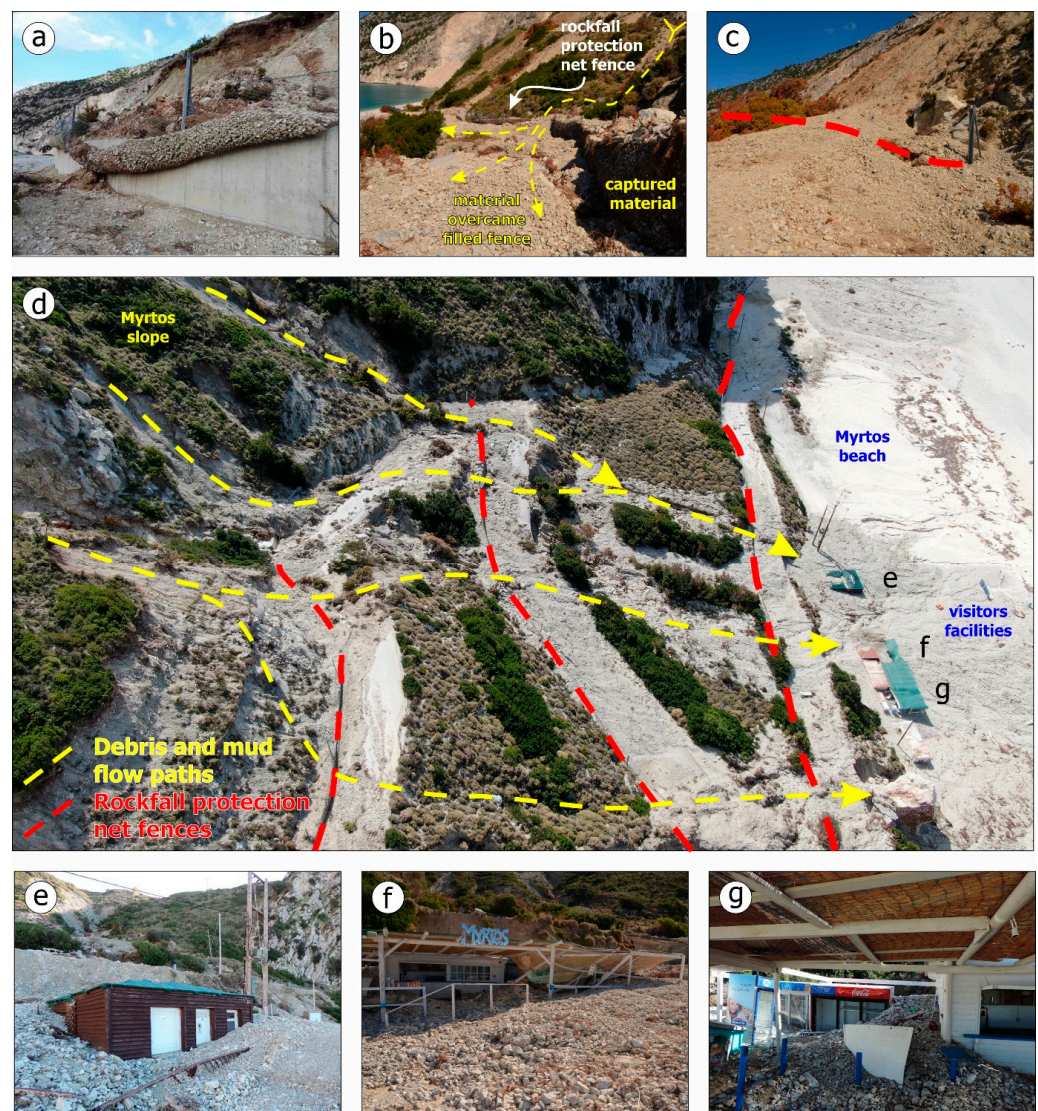


Figure 6. Characteristic views of (a–g) the impact of the debris and mud flows generated by Medicane Ianos on the rockfall protection net fences (a–d) and the visitor facilities along the beach (d–g). The slope protection works were disabled in several sites due to the large quantity of mobilized material, which partially covered large segments of the road (d) and also the tourist facilities and infrastructure at the base of the slope (e–g), which were almost buried in the deposits.

3. Data and Methods

The first out of two flight surveys was carried out before the medicane, more specifically on 18 July 2020 (Figure 7), using a commercial multi-rotary UAS (DJI Phantom 4 RTK) (Figure 7a), which carries a global navigation satellite system (GNSS) antenna with the ability of real-time kinematics (RTK) processing (Figure 7b). The same equipment was used also for the post-medicane survey, which was carried out on October 6th, 2020 (Figure 7). The surveys were planned as part of the project “LAERTIS—Innovative Risk Management System in the Region of Ionian Islands” (MIS: 5010951) funded by the European Union under the National Strategic Reference Framework. To acquire comparable data, we repeated the survey at the same location (Figure 8).

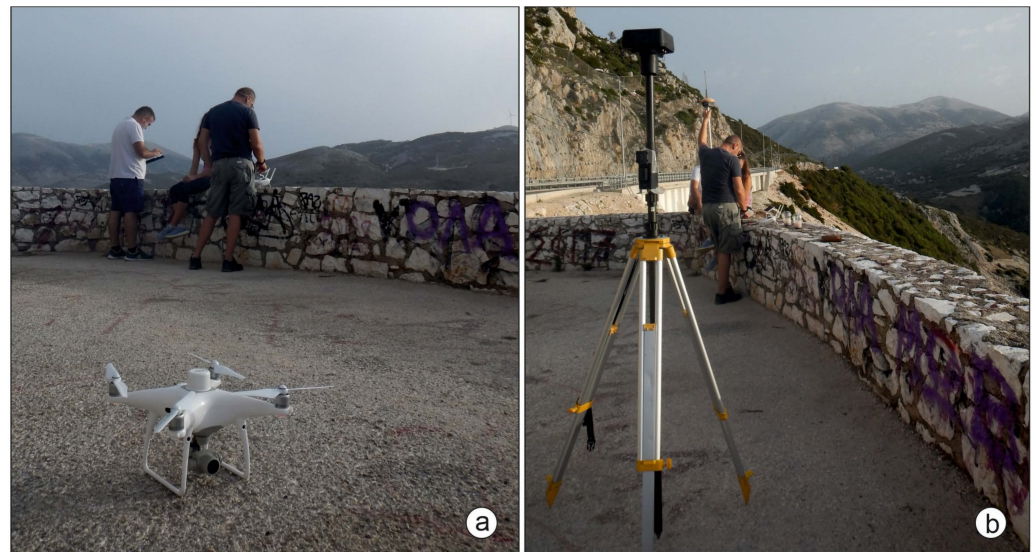


Figure 7. Views of the equipment used for detecting the geomorphological changes triggered by the 2020 Medicane Ianos in the Myrtils coastal area: (a) a commercial multi-rotary UAS (DJI Phantom 4 RTK) with an on-board GNSS antenna with the ability of RTK processing was used as a rover antenna, (b) the DJI D-RTK-2 was used as the base station antenna.

The aim of the multi-temporal UAS data collection and analysis was to create a series of digital surface models (DSMs) of the studied slope, along with orthophotomosaics, based on the structure-from-motion technique [33,74]. By comparing these multi-temporal photogrammetric results it was possible to quantify the topographic changes of the studied surface.

Although the same flight properties were used (path, elevation, and camera angle), the total number of acquired photographs was slightly different in the two surveys (Table 1), attributed to differences in satellite geometry during the flights, which in turn affects the UAS camera positioning, as well as the weather (wind direction and amplitude). Nevertheless, this is not considered to affect the overall methodology and the results. It took several flights to plan the flying strategy to satisfactorily cover the entire study area, due to the steep topography of the slopes surrounding the beach. A DJI Phantom 4 RTK UAS was operated at a maximum of 385 m above sea level (ASL) after it was launched from a suitable take-off area located at a beach view balcony located at 330 m ASL (Figure 7a). The covered area was about 1.2 km².

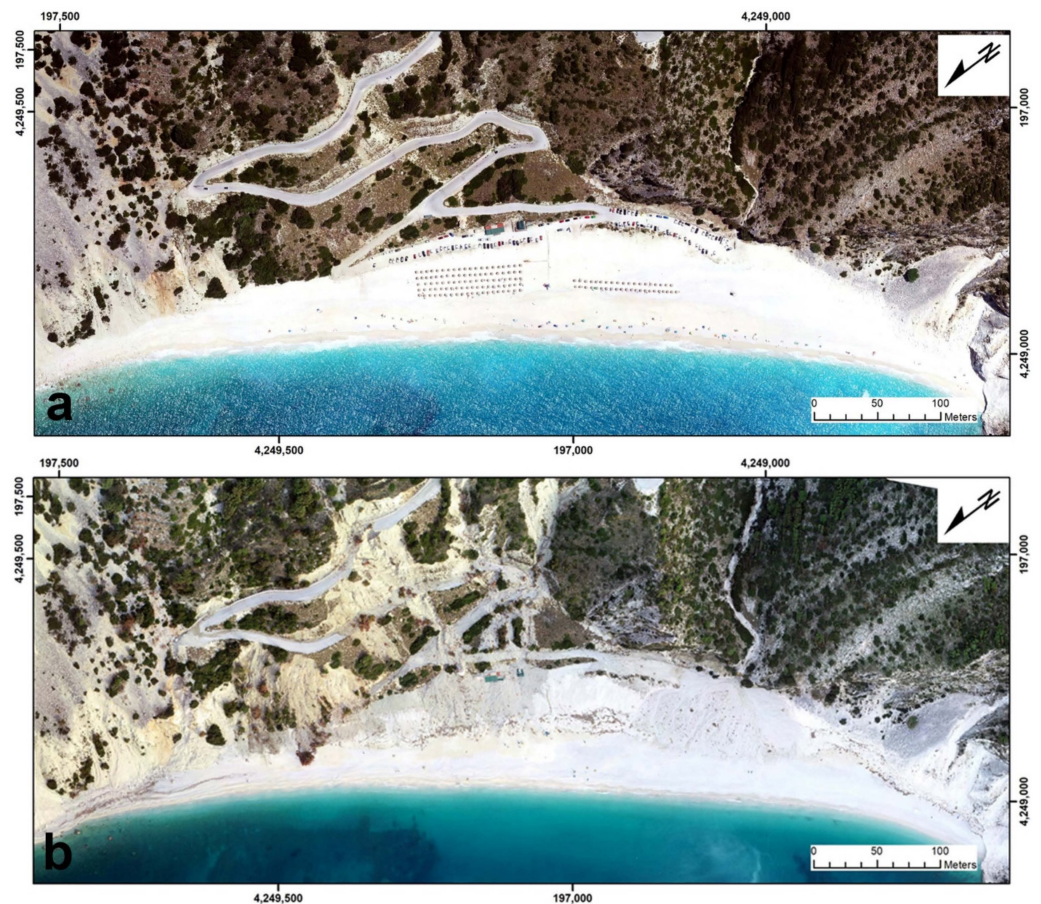


Figure 8. Overview of the geomorphic changes at the popular Myrtos beach, through comparison of the constructed orthoimages before (a) and after (b) the Mediane Ianos disaster.

Table 1. Details of the photogrammetric processing of the two surveys.

	July 2020 Survey			October 2020 Survey		
Flying altitude	375m			383m		
Number of images	595			451		
Overlap	80%			80%		
Dense point cloud	~77 million points			~54 million points		
Camera location RMS error	X(m)	Y(m)	Z(m)	X(m)	Y(m)	Z(m)
	1.19	1.98	1.57	0.003	0.004	0.007
GCPs RMS error	X(m)	Y(m)	Z(m)	X(m)	Y(m)	Z(m)
	0.03	0.07	0.07	0.03	0.07	0.07

The onboard GNSS receiver, antenna, and inertial measurement unit (IMU) calculate the absolute camera positions and altitudes directly with high-accuracy measurements [75,76]. The preflight planning included the setup of the flight routes and elevation above the take-off area, the image acquisition angle, the front and side overlap between the successive aerial photographs, the UAS speed during the flight, as well as the camera function details. Additionally, setting up the connectivity with the GNSS base station network was also a crucial point for taking advantage of the RTK ability, and consequently increased the positioning accuracy during the data acquisition phase, even if the error would be largely minimized during the photogrammetric processing phase.

The quality of the camera (FC6310R, 20Mpx, 8.8 mm focal length) did not require the UAS to stop at waypoints to take oriented photographs to avoid motion blur in images due to possible short-term compensating UAS movements; therefore, it was not necessary to exclude many photographs at the quality control phase. The highest resolution obtained

was 6–8 cm through an effort to keep the ground sampling distance (GSD) as low as possible due to the site topography that was characterized by sharp relief. This resolution was rather satisfactory for the specific use of the final products. The images were acquired with the camera set at an off-nadir position, and this 90° angle was steady due to the UAS built-in gimbal. The flight plan was set to keep an image overlap of 80% forward and 80% side, as this was calculated by the flight mission software.

Photogrammetric processing was carried out twice, for the pre-and post-medicane surveys. It was based on the SfM photogrammetrical approach and implemented using the commercial software Agisoft Metashape Professional (1.7.5 build 13229) [77]. The processing required the alignment of the aerial images and the creation of a sparse point cloud followed by a regular mesh generation, which was used in both flight surveys.

The differentiation between the two projects comes right afterward at the processing workflow and it has to do with the co-registration of the results of the two periods (before and after the medicane damages) and the need for higher precision of both outcomes. Several techniques, each one with pros and cons, were used for the determination of surface deformation features, as well as for the calculation of changes within the prone area covered by mudflows accompanied by volumetric differences from the multi-temporal DSMs [78].

Therefore, we chose the post-medicane survey as the reference project since the non-destructed areas could be identified in both projects and used as tie-points between them. This is a very important barrier that needs to be overcome to create a successive multi-temporal image after co-registering the final products very accurately [79].

We chose the post-processing kinematics (PPK) approach for georeferencing, by including GNSS permanent station RINEX data within the procedure [80]. The succeeded accuracy was more than satisfactory, reaching horizontal and vertical errors in the order of 0.009 m, yielding a very reliable dataset from the geolocation point of view.

The procedure continued with generating a dense point cloud, therefore creating much finer topographic details. At a later step, texturing was also applied before generating the final ortho-image as well as the DSM [81]. Even though the NRTK approach was also chosen for the earliest survey, the need for co-registration led us to also use ground control points (GCPs) within the processing. By applying this technique, we managed to succeed the highest precision between the two projects by picking seven points on the post-disaster ortho-image which remained unchanged after the medicane and using them as pseudo-GCPs [82] during the photogrammetric procedure of the pre-disaster project (Figure 9).

The pseudo-GCPs were used in the reference dataset to easily bring the target dataset to the exact same position with an error of 0.007 m, which is rather satisfactory. The post-medicane orthoimage was used for recording the X and Y coordinates, whilst the interpolated DSM was used for the extraction of every GCP elevation.

Photogrammetric processing of both surveys led to the production of high-quality dense point clouds, consisting of about 75,000,000 points each (Table 1). Each point of the cloud includes information about the reflectance in the visible (RGB) spectra along with X, Y, and Z coordinates [33].

By making spatial raster calculations between multi-temporal DSMs of the same study area, especially when acquired after a specific event that has significantly altered the surface morphology (e.g., floods, earthquakes, and mass movement), a new dataset called “DSM of Difference” can be created. The latter may be used for the quantification of any spatial alterations due to the effect of the natural event on the study area’s morphology [83]. Volumes of moved material can be calculated, providing useful information for researchers on the damage control and the protection measures that should be implemented for further fortification of the affected area to prevent similar disasters in the future.

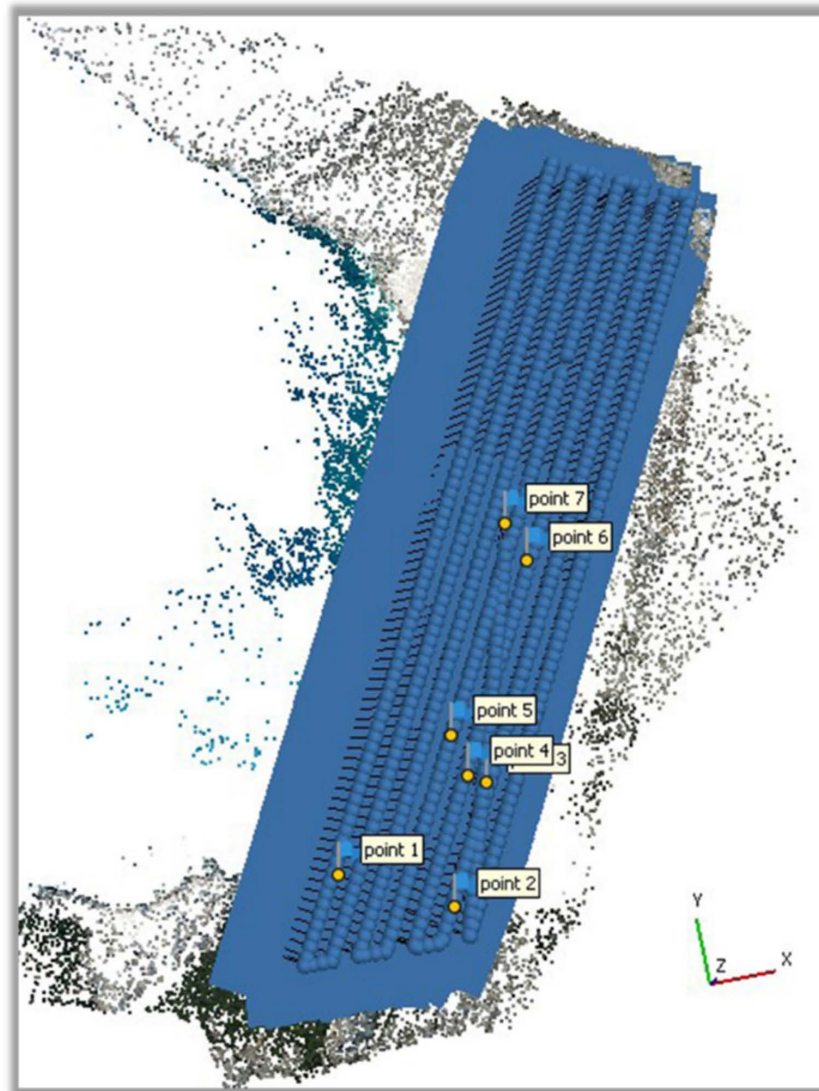


Figure 9. Sparse point cloud showing the UAS camera locations during the image acquisition and the position of the seven pseudo-GCPs.

4. Results

The analysis shows that within the time period studied (between July and October 2020) a significant change has occurred, attributed to the Mediane Ianos event, as based on rainfall and earthquake data, no other important event occurred in this period.

The survey showed that a large part of the slope, which hosts the roadway that leads to the waterfront and the beach area itself, together with several retaining walls, was covered by debris flows from higher up the slope. Distinct instabilities across the study site were visible in the DoD output, including debris cones and extensive mudflows triggered by the high-intensity rainfall of the Ianos event. Based on the approach followed, it was possible to delineate the activated area and measure it through comparison of the ortho-photographs, allowing the precise calculation of the magnitude of the area that was covered with debris. A high-resolution comparison between the two DSMs (performed by using the ArcGIS add-in algorithm, called geomorphic change detection, or GCD) [84]) illustrated noteworthy elevation changes (shown in Figure 10).

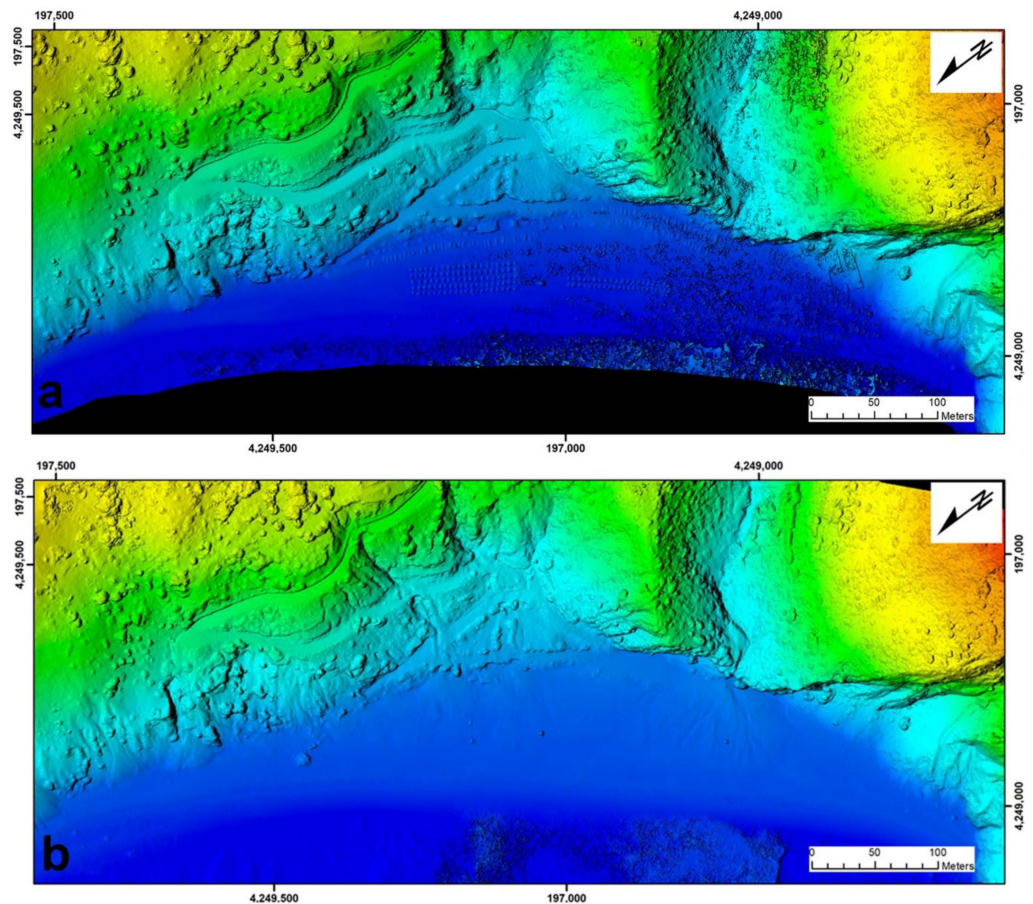


Figure 10. Comparison of digital surface models created from imagery captured (a) before and (b) after the destructive event.

This observation in turn led to detailed area and volume calculations using the DoD method [83,85] (shown in Figure 11), providing results with an accuracy in the order of a few centimeters. Specifically, we determined that the total area that suffered changes due to the storm was 59,418.60 m², of which 40,678.20 m² was covered with debris (mostly in the central section of the area). Furthermore, an area of 6,618.25 m², situated along the parking lot near the beach, was covered with debris, blocking the outlet of a small stream draining part of northwest Cephalonia (Figure 11).

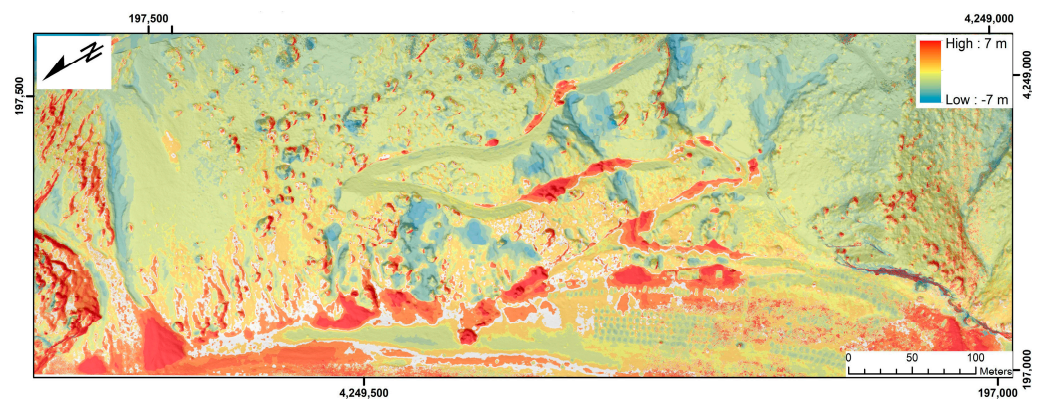


Figure 11. The results of the processing of the affected area over Myrtos beach with the DoD technique. The color scale shows the calculated vertical changes. Blue areas show elevation loss (erosion) and therefore the sources of material, whereas red areas of the figure show elevation gain (deposition), which in many locations exceeds a thickness of 5 m.

The total change in terms of volume was calculated to be 45,575.05 m³ (with an uncertainty of ± 8247.79 m³). The larger portion of this change in terms of volume was associated with a flow of debris in the central part of the study site. Around this location, the elevation values recorded in the pre-and post-Ianos event DSMs were found to be quite modified, either negatively (erosion) or positively (deposition). It was calculated that a volume of 15,318.73 (± 3158.05) m³ was deposited at new locations within Myrtos beach and 30,256.33 (± 5089.74) m³ was removed from its original location after Ianos.

Detection of vertical changes allows the delineation of areas with erosion and scouring, as well as areas with deposition. In fact, a comparison of observations and phenomena after the seismic sequence in Cephalonia in early 2014 [47] with change detection results from the present study reveals that the greatest impact from the occurrence of both phenomena was located in the same segments of the slope. In particular, it was found that the paths followed by the debris flows in the Medicane Ianos event correspond with the paths followed by the rock fragments that were detached from the slope during the 2014 earthquakes, before they ended up at the base of the slope, a few tens of meters from the shore [47]. In the study site, taking into account the geological and tectonic setting, it can be argued that the synergy of the tectonic deformation of the area, the mechanical characteristics of the geological formations in Myrtos slope, and the strong ground motion in 2014 resulted in the creation of selective displacement paths of unstable materials, which were roughly followed again during Ianos a few years later. In particular, the presence of an oblique-slip reverse fault crossing the coastal area of Myrtos, placing the southern part of the Erissos Peninsula fault block on top of the northern part of the Aenos fault block, and the formation of springs at various sites on the slope have formed unfavorable conditions (heterogeneity, anisotropy, fragmentation, and low coherence) for maintaining the stability of the slope [49,50]. This stability is repeatedly disturbed during the occurrence of not only geophysical hazards (e.g., 1953, 1983, and 2014 earthquakes) but also hydro-meteorological hazards (2020 Medicane Ianos), resulting in failures in the parts of the slope particularly prone to such phenomena.

Furthermore, we compared the results of the above methodology and the field observations acquired from post-event field surveys in the affected area; after the 2014 Cephalonia earthquakes [47] and after Medicane Ianos [70]. The comparison shows that the areas where rocks were deposited during the 2014 earthquake-triggered landslides are identical to the areas where the maximum accumulation of unstable materials from the 2020 rock flows occurred. Based mainly on field observations and secondarily from the analysis of the results of the above approach, it was found that the rockfall protection, which was constructed after the seismic sequence in early 2014, failed during Medicane Ianos. They were unable to retain the mobilized material created during the rainfall and subsequently during flows. As a result, the unstable material passed over the protective barriers and fences and deposited at several points along the road network leading from the main road to Myrtos beach. Most of it was deposited on the flat part of the beach near the base of the slope, with a maximum thickness of the deposition exceeding 5 m, as previously mentioned.

5. Discussion

This work explores the capabilities of UAS-aided surveys in the field of slope failures and shallow instabilities as a novel tool aiming to improve our understanding of identifying, delineating, and measuring these phenomena.

The findings show that a UAS-aided post-event investigation is an effective and practical method able to extract the geometric properties of the slope and the mass movement processes with accuracy and identify failure surfaces, deposits, scarps, high-risk areas, and other morphological characteristics in a quantified way. The findings support and build on recent research in the field of detailed mapping of geomorphological features [86,87] through a range of either manual or automated techniques [88], and demonstrate the strengths and weaknesses of the application.

Concerning the advantages of the current approach, it has to be noted that in the course of a UAS-aided survey, the investigation follows a different sequence of steps compared to a more traditional approach, for example in a d-GNSS survey. In the latter, the local morphology can be described through pre-organized cross-sections or paths across or around the deposits, accompanied by photos from certain locations. In contrast, in the UAS-aided approach, the survey team collects data from a wider area, obtaining accurate morphometric information from a larger part of the slope. This allows not only for a more complete measurement coverage of the phenomena but also for a better understanding of the surrounding environment in which they occur (including its morphology, infrastructure, exposed assets, processes, etc.), as photogrammetry allows the processing of multiple parts of the study site, allowing greater flexibility in site examination.

In addition, with respect to data collection, a UAS-aided survey can acquire data that can be stored and re-examined after the field survey. The storage of terrain data allows the research team to revisit the study site virtually, even in the future, providing flexibility in scheduling data collection and data analysis. This can be particularly advantageous in the case of unsafe or remote sites or areas with restricted access, conditions which are not rare in locations with ongoing crises. It can be also useful to protect surveys from data loss from disruption of terrain elements (e.g., due to clean-up), preserving observations. Furthermore, the use of UAS permits capturing data from a site with minimum requirements regarding time and personnel as well as concerns regarding safety and access. In addition, during data collection, there is very limited disruption to visitors or clean-up personnel and authorities. Overall, these characteristics facilitate research and its applications in civil protection, without facing common practical limitations associated with post-disaster environments acknowledged in the literature [89].

Furthermore, the high resolution of the model allows qualitative observations on the role of various factors including geological formations and vegetation conditions and their spatial relationship with the observed phenomena. For example, it can be observed whether the sediment sources due to erosion occur across all lithologies found in the study site or only some of them. In addition, the highly detailed model allows observations on the condition of manmade objects and infrastructure and can assess their role or their position in relation to the hydro-geomorphic phenomena. Especially when the C2C method [90,91] is applied effectively, i.e., the two point-clouds are successfully co-registered (by using common GCPs), a very high-resolution result is accomplished (Figure 11). Based on the latter approach, one can distinguish which parts of the road are subject to debris deposition or which buildings/structures are within the debris flow deposition areas. For instance, in the present case, we identified important areas of erosion upslope of the beach and showed that parts of the access road, the parking area, and the local convenience stores are situated within the erosion and deposition areas. Figure 12 illustrates these observations in detail, delineating zones throughout the study sites.

Examination of the vertical changes shows clearly that the road leading to the site was covered in debris from upstream in many locations, while large mudflows, rock avalanches, and debris cones are revealed, as the results indicate connections between the source and the final deposition locations of the sediments. The C2C method led to a quite detailed temporal change (before and after the Ianos extreme event) based on the two point-cloud elevation differences (Figure 13).

Given the very high intensity of the event, the unaffected areas, which can be distinguished using the current application (see Figure 12), can be considered as the parts of the site that have a lower risk of mass movement phenomena, whereas the affected areas can be delineated as risk-prone. This distinction can be further fine-tuned with continuous monitoring of a site and can become the basis for sustainable development, in the sense that it allows undisrupted usage through an in-depth understanding of risk. This in turn allows the adaptation of the existing uses of the site taking into consideration risk level zonation.

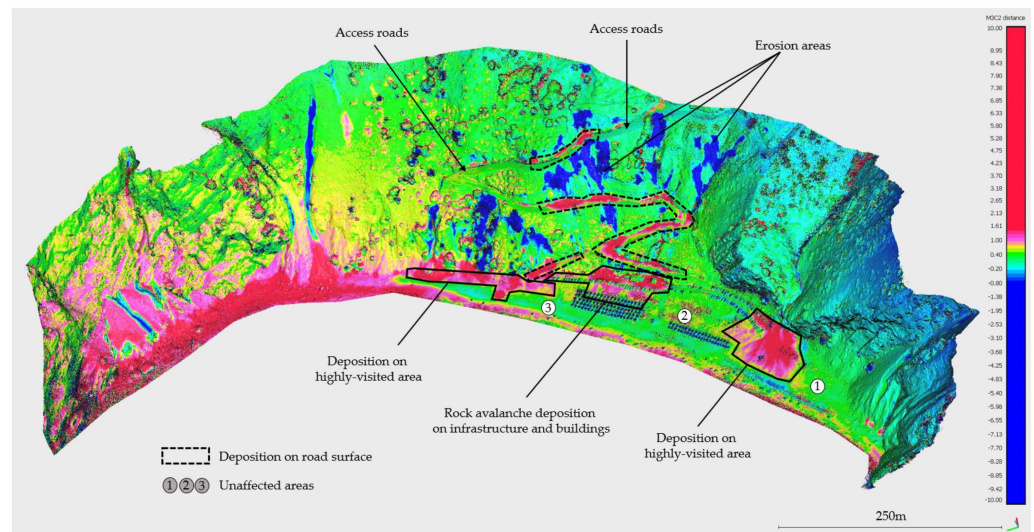


Figure 12. A perspective pseudo-3D view of the affected area, with a color scale showing vertical changes (erosion and deposition), and the distinctly affected elements (including high-visitation areas, infrastructure, and buildings), parts of the access road that suffered deposition from debris flows and rock avalanches, indicating the higher risk parts of the site, as well as the unaffected areas of Myrtos.

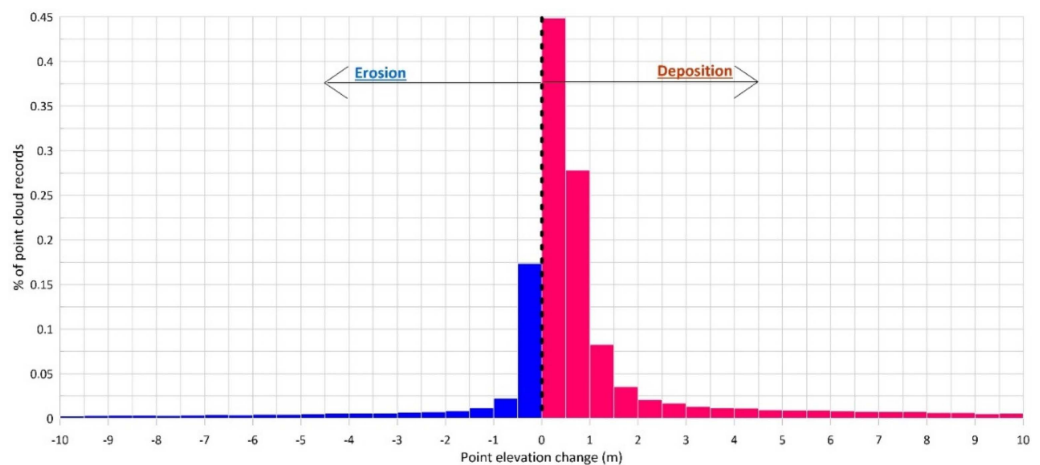


Figure 13. Graph showing the percentage of the points from the point cloud that have either increased their elevation (red bars) showing deposition or decreased their elevation (blue bars) showing erosion.

One other advantage of the use of a UAS is the availability of on-demand imagery, in comparison for example with satellites that, although very effective, have limitations due to cloud canopy or image unavailability due to satellite period, etc. The resolution of UAS-derived imagery can be significantly higher than satellite images even using consumer-grade equipment.

Within the frame of co-registration, it is a scientific principle that in order to succeed accurate intercomparison, an accurate georeferencing is needed. The most prevalent georeferencing method, the use of ground control points (GCPs), is a very reliable method; however, the necessity to be evenly distributed in addition to the morphological challenges of the terrain can make the GCP method time-consuming and unreliable concerning the position uncertainty over time. Considering the fact that the morphological changes must be monitored due to extreme weather events, it is sadly difficult to control the locations of the GCPs contingent on the weather impact and the surface deformations. Studies have shown that the results of photogrammetry applications compete in practicality and accuracy with the more common and costly terrestrial laser scanning approaches [92,93].

With regard to limitations, in general, the altitude is inversely proportional to the distinctive shooting ability of the camera; therefore, the altitude should be adapted concerning the required resolution and the extent of the site under study. In this sense, the user should always select the technique by keeping in mind that there is a tradeoff between study area size and resolution, calculating available time by considering safety and equipment characteristics. In addition, the actual aircrafts used to capture the data are sensitive to strong winds and rain, which are both not uncommon between or after storm incidents, especially in winter and autumn months. Bad weather may prohibit aerial surveys. Moreover, vegetation canopies can be an obstacle in this application, as they can appear as a false terrain surface in photogrammetric analysis. In particular, the issue can manifest if dense and tall vegetation that is present before the event has been affected by the mass movement phenomena during the event. In this case, it can lead to an overestimation of changes in the DoD; therefore, attention should be paid to the results in such locations by using vegetation removal or filtering [40,41]. In the present application, there was no such problem since the vegetation was sparse and low. Finally, it has to be noted that additional difficulty comes from the handling of large datasets and the requirements in terms of computational resources to reduce processing time.

Overall, the findings indicate that a sequence of a UAS-derived imagery series in the form of continuous or regular monitoring can be particularly useful to monitor the earth's surface gravitational processes and their evolution [94,95]. Particularly in the case of highly visited coastal areas, it can also delineate high-risk areas providing a better understanding of where safety is compromised. In this sense, an important practical implication of using UAS-derived monitoring of slopes is that it can be useful in microzonation of areas of interest, to offer a better balance between retaining safety of users/visitors but at the same time allowing the use of the site so that it will continue to support the development of a region in a more sustainable framework.

Taking into account the previous discussion, during the design and selection of slope failure protection works, it is imperative to take into account the type and properties of failures that may be caused by the occurrence of not only geophysical (earthquakes) but also hydro-meteorological hazards (rainfall), in order to increase the safety factor of the slope and to achieve a safe stay of visitors in the area. It is important to note that both the seismic sequence in early 2014 and Medicane Ianos occurred during the winter and autumn seasons, respectively, i.e., during periods when traffic in the coastal area of Myrtos and particularly on its beach was limited.

Furthermore, another useful point emerges from this application. In an area that is already known for its susceptibility to landslides (Myrtos has been characterized as an area of critically high susceptibility to landslides [50]), individual susceptible segments can be defined with greater precision and mapped with higher resolution using the proposed approach. By highlighting these areas (Figure 12), the authorities involved in the prevention and management of disasters induced by natural hazards have at their disposal a valuable tool for taking effective measures to limit the adverse conditions and the unpleasant impact on the local population and visitors, as well as on the existing adjacent buildings, networks, and infrastructure. Furthermore, they can select segments of low susceptibility to slope failure and use them for safe accommodation, for expanding related facilities and infrastructure, or any other use appropriate for such a valuable highly visited site.

The highly detailed observations allowed by the proposed approach were a unique opportunity to shed light on the synergy between hydro-geomorphic processes and the active tectonic deformation of rock formations, showing the strong relationship between geological and tectonic characteristics and erosion/sedimentation processes which continuously shape the landscape.

6. Conclusions

This application shows that UASs can be an important addition in surveys of geomorphological processes, providing an efficient, rapid, and accurate way of performing terrain

observations, detecting changes in a post-extreme event environment, and allowing for a deeper understanding of how these processes work.

The presented approach has a range of advantages. It was shown to be especially helpful for studying a site on demand with minimum disruption and requirements during the post-disaster period. In addition, although these capabilities are appropriate in the context of monitoring disaster events and mapping their impact on the natural and built environment, the efficiency of this application is an important indicator that they can function in a continuous monitoring scheme in a framework of systematically repeated surveys.

The described UAS-based methodology presents a quite simple and convenient way of comparing datasets from different time periods and achieving a co-registration of very high accuracy. The accuracy in the final photogrammetric product—including the co-registration between multi-temporal datasets—proved to be very crucial in terms of accurate measurement of distances between the original point clouds and eventually the volume of mass movement through mudflows, which leads consequently to the quantification of the surface alteration.

On this basis that the application allows accurate observations of erosion and deposition processes, volumetric estimates of the geomorphic changes and the delineation of the affected and the unaffected areas were obtained. Both methods, either C2C or DoD, provide realistic and reliable results in terms of the quantification of surface material relocation. Detailed change detection, along with the volume calculations, are much more effective with the use of photogrammetric techniques, as long as the dataset co-registration procedure is successful and accurate.

Overall, the complexity of mass wasting processes in light of the threat of climate change, together with the high vulnerability of the region (particularly highly visited areas), show that there is a need for a better understanding of the risks of slope failures and various instabilities caused by extreme weather events. UASs have the potential to contribute to monitoring these effects and improve our understanding of the geomorphic processes. The high-resolution of results allows for microzonation of a study area, which is the foundation for allowing these high-value sites to be able to retain their use and their socio-economic activities with minimum disruption, while at the same time keeping high standards of safety. New technologies, such as the one applied in the present study, provide such solutions with certain limitations and can be an important step toward sustainable development.

Author Contributions: Conceptualization, E.V. and S.M.; methodology, E.V., E.K., A.K., S.L. and C.F.; software, E.V., E.K. and A.K.; validation, E.V., E.K. and A.K.; formal analysis, E.V., M.D., S.M. and A.K.; investigation, E.V., E.K., A.K., S.L. and C.F.; resources, E.V.; data curation, E.V. and A.K.; writing—original draft preparation, E.K., E.V., M.D., S.M. and E.L.; writing—review and editing, E.K., E.V., M.D. and S.M.; visualization, E.V., E.K., A.K., S.L. and M.D.; funding acquisition, E.L. All authors have read and agreed to the published version of the manuscript.

Funding: This research was funded by the “LAERTIS—Innovative Risk Management System in the Region of Ionian Islands” project included in the Priority Axis “Environmental Protection and Sustainable Development” of the Regional Operational Programme “Ionian Islands 2014–2020” (grant number MIS: 5010951), which is funded by the European Regional Development Fund (ERDF) and National Resources under the National Strategic Reference Framework (NSRF) 2014–2020.

Institutional Review Board Statement: Not applicable.

Informed Consent Statement: Not applicable.

Data Availability Statement: Not applicable.

Acknowledgments: The present work was performed within the project “LAERTIS—Innovative Risk Management System in the Region of Ionian Islands” (MIS: 5010951) funded by the European Union under the National Strategic Reference Framework. The authors highly appreciate the constructive comments of the three anonymous reviewers, which increased the quality of the initially submitted manuscript.

Conflicts of Interest: The authors declare no conflict of interest.

References

1. Petley, D. Global patterns of loss of life from landslides. *Geology* **2012**, *40*, 927–930. [[CrossRef](#)]
2. Glade, T. Landslide occurrence as a response to land use change: A review of evidence from New Zealand. *Catena* **2003**, *51*, 297–314. [[CrossRef](#)]
3. Tapas, M.R.; Priyom, R.; Ritwik, M.; Govindharaj, K.B.; Kumar, K.V. Spatial characteristics of landslides triggered by the 2015 Mw 7.8 (Gorkha) and Mw 7.3 (Dolakha) earthquakes in Nepal. *Landslides* **2017**, *14*, 697–704. [[CrossRef](#)]
4. Meunier, P.; Uchida, T.; Hovius, N. Landslide patterns reveal the sources of large earthquakes. *Earth Planet. Sci. Lett.* **2013**, *363*, 27–33. [[CrossRef](#)]
5. ur Rahman, A.; Khan, A.N.; Collins, A.E. Analysis of landslide causes and associated damages in the Kashmir Himalayas of Pakistan. *Nat. Hazards* **2014**, *71*, 803–821. [[CrossRef](#)]
6. Widiyanto, W.; Santoso, P.; Hsiao, S.-C.; Imananta, R. Post-event Field Survey of 28 September 2018 Sulawesi Earthquake and Tsunami. *Nat. Hazards Earth Syst. Sci.* **2019**, *1*, 1–23. [[CrossRef](#)]
7. Budimir, M.E.A.; Atkinson, P.M.; Lewis, H.G. Earthquake-and-landslide events are associated with more fatalities than earthquakes alone. *Nat. Hazards* **2014**, *72*, 895–914. [[CrossRef](#)]
8. Bird, J.F.; Bommer, J.J. Earthquake losses due to ground failure. *Eng. Geol.* **2004**, *75*, 147–179. [[CrossRef](#)]
9. Haque, U.; da Silva, P.F.; Devoli, G.; Pilz, J.; Zhao, B.; Khaloua, A.; Wilopo, W.; Andersen, P.; Lu, P.; Lee, J.; et al. The human cost of global warming: Deadly landslides and their triggers (1995–2014). *Sci. Total Environ.* **2019**, *682*, 673–684. [[CrossRef](#)]
10. Haque, U.; Blum, P.; da Silva, P.F.; Andersen, P.; Pilz, J.; Chalov, S.R.; Malet, J.P.; Auflič, M.J.; Andres, N.; Poyiadji, E.; et al. Fatal landslides in Europe. *Landslides* **2016**, *13*, 1545–1554. [[CrossRef](#)]
11. Gariano, S.L.; Guzzetti, F. Landslides in a changing climate. *Earth-Sci. Rev.* **2016**, *162*, 227–252. [[CrossRef](#)]
12. Borga, M.; Stoffel, M.; Marchi, L.; Marra, F.; Jakob, M. Hydrogeomorphic response to extreme rainfall in headwater systems: Flash floods and debris flows. *J. Hydrol.* **2014**, *518*, 194–205. [[CrossRef](#)]
13. Jones, J.N.; Boulton, S.J.; Bennett, G.L.; Stokes, M.; Whitworth, M.R.Z. Temporal Variations in Landslide Distributions Following Extreme Events: Implications for Landslide Susceptibility Modeling. *J. Geophys. Res. Earth Surf.* **2021**, *126*, 1–26. [[CrossRef](#)]
14. Korup, O.; Clague, J.J. Natural hazards, extreme events, and mountain topography. *Quat. Sci. Rev.* **2009**, *28*, 977–990. [[CrossRef](#)]
15. Scorpio, V.; Crema, S.; Marra, F.; Righini, M.; Ciccacese, G.; Borga, M.; Cavalli, M.; Corsini, A.; Marchi, L.; Surian, N.; et al. Basin-scale analysis of the geomorphic effectiveness of flash floods: A study in the northern Apennines (Italy). *Sci. Total Environ.* **2018**, *640*, 337–351. [[CrossRef](#)] [[PubMed](#)]
16. Guzzetti, F.; Peruccacci, S.; Rossi, M.; Stark, C.P. The rainfall intensity-duration control of shallow landslides and debris flows: An update. *Landslides* **2008**, *5*, 3–17. [[CrossRef](#)]
17. Salvati, P.; Bianchi, C.; Rossi, M.; Guzzetti, F. Societal landslide and flood risk in Italy. *Nat. Hazards Earth Syst. Sci.* **2010**, *10*, 465–483. [[CrossRef](#)]
18. Nastos, P.T.; Dalezios, N.R. Preface: Advances in meteorological hazards and extreme events. *Nat. Hazards Earth Syst. Sci.* **2016**, *16*, 1259–1268. [[CrossRef](#)]
19. Nastos, P.T.; Dalezios, N.R.; Faraslis, I.N.; Mitrakopoulos, K.; Blanta, A.; Spiliotopoulos, M.; Sakellariou, S.; Sidiropoulos, P.; Tarquis, A.M. Risk management framework of environmental hazards and extremes in Mediterranean ecosystems. *Nat. Hazards Earth Syst. Sci.* **2021**, *21*, 1935–1954. [[CrossRef](#)]
20. Martha, T.R.; Roy, P.; Govindharaj, K.B.; Kumar, K.V.; Diwakar, P.G.; Dadhwal, V.K. Landslides triggered by the June 2013 extreme rainfall event in parts of Uttarakhand state, India. *Landslides* **2015**, *12*, 135–146. [[CrossRef](#)]
21. Lionello, P. *The Climate of the Mediterranean Region. From the Past to the Future*; Lionello, P., Ed.; Elsevier: Amsterdam, The Netherlands, 2012; ISBN 9780124160422.
22. Zittis, G.; Almazroui, M.; Alpert, P.; Ciais, P.; Cramer, W.; Dahdal, Y.; Fnais, M.; Francis, D.; Hadjinicolaou, P.; Howari, F.; et al. Climate Change and Weather Extremes in the Eastern Mediterranean and Middle East. *Rev. Geophys.* **2022**, *60*, 762. [[CrossRef](#)]
23. IPCC Climate Change 2013: The Physical Science Basis. *Contribution of Working Group I to the Fifth Assessment Report of the Intergovernmental Panel on Climate Change*; Cambridge University Press: Cambridge, UK, 2013.
24. Romero, R.; Emanuel, K. Climate change and hurricane-like extratropical cyclones: Projections for North Atlantic polar lows and medicanes based on CMIP5 models. *J. Clim.* **2017**, *30*, 279–299. [[CrossRef](#)]
25. González-Alemán, J.J.; Pascale, S.; Gutierrez-Fernandez, J.; Murakami, H.; Gaertner, M.A.; Vecchi, G.A. Potential Increase in Hazard From Mediterranean Hurricane Activity With Global Warming. *Geophys. Res. Lett.* **2019**, *46*, 1754–1764. [[CrossRef](#)]
26. Cavicchia, L.; Von Storch, H.; Gualdi, S. Mediterranean tropical-like cyclones in present and future climate. *J. Clim.* **2014**, *27*, 7493–7501. [[CrossRef](#)]

27. Gaertner, M.A.; Jacob, D.; Gil, V.; Domínguez, M.; Padorno, E.; Sánchez, E.; Castro, M. Tropical cyclones over the Mediterranean Sea in climate change simulations. *Geophys. Res. Lett.* **2007**, *34*, 1–5. [[CrossRef](#)]
28. Taussik, J. Development Plans and the Coastal Zone Author(s). *Town Plan. Rev.* **1996**, *67*, 397–420. [[CrossRef](#)]
29. Gormsen, E. The impact of tourism on coastal areas. *GeoJournal* **1997**, *42*, 39–54. [[CrossRef](#)]
30. Mavromatidi, A.; Briche, E.; Claeys, C. Mapping and analyzing socio-environmental vulnerability to coastal hazards induced by climate change: An application to coastal Mediterranean cities in France. *Cities* **2018**, *72*, 189–200. [[CrossRef](#)]
31. Bosom, E.; Jiménez, J.A. Probabilistic coastal vulnerability assessment to storms at regional scale—Application to Catalan beaches (NW Mediterranean). *Nat. Hazards Earth Syst. Sci.* **2011**, *11*, 475–484. [[CrossRef](#)]
32. Vassilakis, E.; Papadopoulou-Vrynioti, K. Quantification of deltaic coastal zone change based on multi-Temporal high resolution earth observation techniques. *ISPRS Int. J. Geo-Information* **2014**, *3*, 18–28. [[CrossRef](#)]
33. Westoby, M.J.; Brasington, J.; Glasser, N.F.; Hambrey, M.J.; Reynolds, J.M. “Structure-from-Motion” photogrammetry: A low-cost, effective tool for geoscience applications. *Geomorphology* **2012**, *179*, 300–314. [[CrossRef](#)]
34. Domazetović, F.; Šiljeg, A.; Marić, I.; Faričić, J.; Vassilakis, E.; Panđa, L. Automated coastline extraction using the very high resolution worldview (WV) satellite imagery and developed coastline extraction tool (CET). *Appl. Sci.* **2021**, *11*, 9482. [[CrossRef](#)]
35. Dietrich, J.T. Riverscape mapping with helicopter-based Structure-from-Motion photogrammetry. *Geomorphology* **2016**, *252*, 144–157. [[CrossRef](#)]
36. Marteau, B.; Vericat, D.; Gibbins, C.; Batalla, R.J.; Green, D.R. Application of Structure-from-Motion photogrammetry to river restoration. *Earth Surf. Process. Landforms* **2017**, *42*, 503–515. [[CrossRef](#)]
37. Westoby, M.J.; Lim, M.; Hogg, M.; Pound, M.J.; Dunlop, L.; Woodward, J. Cost-effective erosion monitoring of coastal cliffs. *Coast. Eng.* **2018**, *138*, 152–164. [[CrossRef](#)]
38. Langhammer, J.; Vacková, T. Detection and Mapping of the Geomorphic Effects of Flooding Using UAV Photogrammetry. *Pure Appl. Geophys.* **2018**, *175*, 3223–3245. [[CrossRef](#)]
39. Smith, M.J.; Pain, C.F. Applications of remote sensing in geomorphology. *Prog. Phys. Geogr.* **2009**, *33*, 568–582. [[CrossRef](#)]
40. Smith, M.W.; Carrivick, J.L.; Hooke, J.; Kirkby, M.J. Reconstructing flash flood magnitudes using “Structure-from-Motion”: A rapid assessment tool. *J. Hydrol.* **2014**, *519*, 1914–1927. [[CrossRef](#)]
41. Andreadakis, E.; Diakakis, M.; Vassilakis, E.; Deligiannakis, G.; Antoniadis, A.; Andriopoulos, P.; Spyrou, N.I.; Nikolopoulos, E.I. Unmanned aerial systems-aided post-flood peak discharge estimation in ephemeral streams. *Remote Sens.* **2020**, *12*, 4183. [[CrossRef](#)]
42. Wilson, J.P.; Gallant, J.C. Digital Terrain Analysis in Terrain Analysis: Principles and Applications. In *Terrain Analysis: Principles and Applications*; John Wiley & Sons: New York, NY, USA, 2000; pp. 1–27.
43. Niethammer, U.; Rothmund, S.; James, M.R.; Travelletti, J.; Joswig, M. Uav-Based Remote Sensing of Landslides. In Proceedings of the International Archives of Photogrammetry, Remote Sensing and Spatial Information Sciences, Newcastle upon Tyne, UK, 21–24 June 2010; Volume 38, pp. 496–501.
44. Devoto, S.; Macovaz, V.; Mantovani, M.; Soldati, M.; Furlani, S. Advantages of using uav digital photogrammetry in the study of slow-moving coastal landslides. *Remote Sens.* **2020**, *12*, 3566. [[CrossRef](#)]
45. Mishra, O.P. Seismic Microzonation Study of South Asian Cities and Its Implications to Urban Risk Resiliency under Climate Change Scenario. *Int. J. Geosci.* **2020**, *11*, 197–237. [[CrossRef](#)]
46. Lewis, J. Housing construction in earthquake-prone places: Perspectives, priorities and projections for development. *Aust. J. Emerg. Manag.* **2003**, *18*, 35–44.
47. Lekkas, E.L.; Mavroulis, S.D. Earthquake environmental effects and ESI 2007 seismic intensities of the early 2014 Cephalonia (Ionian Sea, western Greece) earthquakes (January 26 and February 3, Mw 6.0). *Nat. Hazards* **2015**, *78*, 1517–1544. [[CrossRef](#)]
48. Lekkas, E.L.; Mavroulis, S.D. Fault zones ruptured during the early 2014 Cephalonia Island (Ionian Sea, Western Greece) earthquakes (January 26 and February 3, Mw 6.0) based on the associated co-seismic surface ruptures. *J. Seismol.* **2016**, *20*, 63–78. [[CrossRef](#)]
49. Mavroulis, S.; Lekkas, E. Revisiting the most destructive earthquake sequence in the recent history of Greece: Environmental effects induced by the 9, 11 and 12 August 1953 Ionian Sea earthquakes. *Appl. Sci.* **2021**, *11*, 8429. [[CrossRef](#)]
50. Mavroulis, S.; Diakakis, M.; Kranis, H.; Vassilakis, E.; Kapetanidis, V.; Spingos, I.; Kaviris, G.; Skourtsos, E.; Voulgaris, N.; Lekkas, E. Inventory of Historical and Recent Earthquake-Triggered Landslides and Assessment of Related Susceptibility by GIS-Based Analytic Hierarchy Process: The Case of Cephalonia (Ionian Islands, Western Greece). *Appl. Sci.* **2022**, *12*, 2895. [[CrossRef](#)]
51. Scordilis, E.M.; Karakaisis, G.F.; Karacostas, B.G.; Panagiotopoulos, D.G.; Comninakis, P.E.; Papazachos, B.C. Evidence for transform faulting in the Ionian sea: The Cephalonia island earthquake sequence of 1983. *Pure Appl. Geophys. PAGEOPH* **1985**, *123*, 388–397. [[CrossRef](#)]
52. Louvari, E.; Kiratzi, A.A.; Papazachos, B.C. The Cephalonia Transform Fault and its extension to western Lefkada Island (Greece). *Tectonophysics* **1999**, *308*, 223–236. [[CrossRef](#)]
53. Sachpazi, M.; Hirn, A.; Clément, C.; Haslinger, F.; Laigle, M.; Kissling, E.; Charvis, P.; Hello, Y.; Lépine, J.C.; Sapin, M.; et al. Western Hellenic subduction and Cephalonia Transform: Local earthquakes and plate transport and strain. *Tectonophysics* **2000**, *319*, 301–319. [[CrossRef](#)]

54. Sakkas, V.; Kapetanidis, V.; Kaviris, G.; Spingos, I.; Mavroulis, S.; Diakakis, M.; Alexopoulos, J.D.; Kazantzidou-firtinidou, D.; Kassaras, I.; Dilalos, S.; et al. Seismological and Ground Deformation Study of the Ionian Islands (W. Greece) during 2014–2018, a Period of Intense Seismic Activity. *Appl. Sci.* **2022**, *12*, 2331. [CrossRef]
55. Lekkas, E.; Danamos, G.; Mavrikas, G. Geological structure and evolution of Kefallonia and Ithaki Islands. *Bull. Geol. Soc. Greece* **2001**, *34*, 11–17. [CrossRef]
56. Lekkas, E.L. *Neotectonic Map—Cephalonia—Ithaki Sheet Scale 1:100,000*; National and Kapodistrian University of Athens: Athens, Greece, 1996.
57. Renz, C. *Die Vorneogene Stratigraphie der normal-sedimentären Formationen Griechenlands*; Institute for Geology and Subsurface Research: Athens, Greece, 1955.
58. Aubouin, J. Contribution à l'étude géologique de la Grèce septentrionale, les confins de l'Épire et de la Thessalie. *Ann. Géol. Pays Hellén* **1959**, *11*, 483.
59. Aubouin, J.; Dercourt, J. Zone préapulienne, zone ionienne et zone du Gavrovo en Peloponnèse occidentale. *Bull. Soc. Géol. Fr.* **1962**, *4*, 785–794. [CrossRef]
60. Underhill, J.R. Triassic evaporites and Plio-Quaternary diapirism in western Greece. *J. Geol. Soc.* **1988**, *145*, 269–282. [CrossRef]
61. BP Co.; University of Munich; Migros, G. *Geological Map of Greece, "Cephalonia Island (Northern and Southern Part)", 1:50000 Scale*; BP: London, UK, 1985.
62. Poscolieri, M.; Lagios, E.; Gregori, G.P.; Paparo, G.; Sakkas, V.A.; Parcharidis, I.; Marson, I.; Soukis, K.; Vassilakis, E.; Angelucci, F.; et al. Crustal stress and seismic activity in the Ionian archipelago as inferred by satellite- and ground-based observations, Kefallinia, Greece. *Geol. Soc. Spec. Publ.* **2006**, *261*, 63–78. [CrossRef]
63. Bartholy, J.; Pongrácz, R.; Pattantyús-Ábrahám, M. Analyzing the genesis, intensity, and tracks of western Mediterranean cyclones. *Theor. Appl. Climatol.* **2009**, *96*, 133–144. [CrossRef]
64. Prezerakos, N.G. The northwest african depressions affecting the south balkans. *J. Climatol.* **1985**, *5*, 643–654. [CrossRef]
65. Nastos, P.T.; Karavana Papadimou, K.; Matsangouras, I.T. Mediterranean tropical-like cyclones: Impacts and composite daily means and anomalies of synoptic patterns. *Atmos. Res.* **2018**, *208*, 156–166. [CrossRef]
66. Kalimeris, A.; Founda, D.; Giannakopoulos, C.; Pierros, F. Long-term precipitation variability in the Ionian Islands, Greece (Central Mediterranean): Climatic signal analysis and future projections. *Theor. Appl. Climatol.* **2012**, *109*, 51–72. [CrossRef]
67. Nastos, P.T.; Matsangouras, I.T. Composite Mean and Anomaly of Synoptic Conditions for Tornadic Days over North Ionian Sea (NW Greece). In *Advances in Meteorology, Climatology and Atmospheric Physics*; Helmis, C.G., Nastos, P.T., Eds.; Springer: Berlin/Heidelberg, Germany, 2012; pp. 639–645. ISBN 9783642291715.
68. Lagouvardos, K.; Karagiannidis, A.; Dafis, S.; Kalimeris, A.; Kotroni, V. Ianos-A Hurricane in the Mediterranean. *Bull. Am. Meteorol. Soc.* **2022**, *103*, E1621–E1636. [CrossRef]
69. Stiros, S.C.; Pirazzoli, P.A.; Laborel, J.; Laborel-Deguen, F. The 1953 earthquake in Cephalonia (Western Hellenic Arc): Coastal uplift and halotectonic faulting. *Geophys. J. Int.* **1994**, *117*, 834–849. [CrossRef]
70. Lekkas, E.; Nastos, P.; Cartalis, C.; Diakakis, M.; Gogou, M.; Mavroulis, S.; Spyrou, N.-I.; Kotsi, E.; Vassilakis, E.; Katsesiadou, K.-N.; et al. Impact of Medicane "IANOS" (September 2020). *Newsl. Environ. Disaster Cris. Manag. Strateg.* **2020**, *20*, 1–140.
71. Eleftheriou, A.; Mouyiaris, N. *Macroseismic reconnaissance in the area of Cephalonia-Zakynthos (Earthquakes 17 & 19-1-83)*; Monograph; Institute of Geological and Mineral Research: Athens, Greece, 1983.
72. Androulidakis, Y.; Makris, C.; Mallios, Z.; Pytharoulis, I.; Baltikas, V.; Krestenitis, Y. Storm surges during a Medicane in the Ionian Sea. In Proceedings of the Marine and Inland Waters Research Symposium, Porto Heli, Greece, 16–19 September 2022; Volume 2, pp. 9–14.
73. Mavroulis, S.; Mavrouli, M.; Lekkas, E. Geological and hydrometeorological hazards and related disasters amid COVID-19 pandemic in Greece: Post-disaster trends and factors affecting the COVID-19 evolution in affected areas. *Saf. Sci.* **2021**, *138*, 105236. [CrossRef]
74. Granshaw, S.I. Structure from motion: Origins and originality. *Photogramm. Rec.* **2018**, *33*, 6–10. [CrossRef]
75. Klingbeil, L.; Eling, C.; Heinz, E.; Wieland, M.; Kuhlmann, H. Direct Georeferencing for Portable Mapping Systems: In the Air and on the Ground. *J. Surv. Eng.* **2017**, *143*, 1–20. [CrossRef]
76. Grayson, B.; Penna, N.T.; Mills, J.P.; Grant, D.S. GPS precise point positioning for UAV photogrammetry. *Photogramm. Rec.* **2018**, *33*, 427–447. [CrossRef]
77. AgiSoft. AgiSoft Metashape Professional 2017. Available online: <https://www.agisoft.com/> (accessed on 24 November 2022).
78. Rossi, G.; Tanteri, L.; Tofani, V.; Vannocci, P.; Moretti, S.; Casagli, N. Multitemporal UAV surveys for landslide mapping and characterization. *Landslides* **2018**, *15*, 1045–1052. [CrossRef]
79. Vassilakis, E.; Fouvelis, M.; Erkeki, A.; Kotsi, E.; Lekkas, E. Post-event surface deformation of Amyntaio slide (Greece) by complementary analysis of Remotely Piloted Airborne System imagery and SAR interferometry. *Appl. Geomat.* **2020**, *13*, 65–75. [CrossRef]
80. Panagiotopoulou, S.; Erkeki, A.; Antonakakis, A.; Grigorakakis, P.; Protopapa, V.; Tsiostras, G.; Vlachou, K.; Vassilakis, E. Evaluation of Network Real Time Kinematics contribution to the accuracy/productivity ratio for UAS-SfM Photogrammetry. In Proceedings of the European Navigation Conference (ENC), Dresden, Germany, 23–24 November 2020; Volume 1, pp. 1–11.

81. Mancini, F.; Dubbini, M.; Gattelli, M.; Stecchi, F.; Fabbri, S.; Gabbianelli, G. Using unmanned aerial vehicles (UAV) for high-resolution reconstruction of topography: The structure from motion approach on coastal environments. *Remote Sens.* **2013**, *5*, 6880–6898. [[CrossRef](#)]
82. Peppas, M.V.; Mills, J.P.; Moore, P.; Miller, P.E.; Chambers, J.E. Automated co-registration and calibration in SfM photogrammetry for landslide change detection. *Earth Surf. Process. Landforms* **2018**, *44*, 287–303. [[CrossRef](#)]
83. Williams, R.D. Section 2.3.2: DEMs of Difference. In *Geomorphological Techniques*; British Society for Geomorphology: London, UK, 2012; pp. 1–17. ISBN 2047-0371.
84. Neverman, A.J.; Fuller, I.C.; Procter, J.N. Application of Geomorphic Change Detection (GCD) to quantify morphological budgeting error in a New Zealand gravel-bed river: A case study from the Makaroro River, Hawke's Bay. *J. Hydrol.* **2016**, *55*, 45–63.
85. Heckmann, T.; Vericat, D. Computing spatially distributed sediment delivery ratios: Inferring functional sediment connectivity from repeat high-resolution digital elevation models. *Earth Surf. Process. Landforms* **2018**, *43*, 1547–1554. [[CrossRef](#)]
86. Fiorucci, F.; Giordan, D.; Santangelo, M.; Dutto, F.; Rossi, M.; Guzzetti, F. Criteria for the optimal selection of remote sensing optical images to map event landslides. *Nat. Hazards Earth Syst. Sci.* **2018**, *18*, 405–417. [[CrossRef](#)]
87. Karantanellis, E.; Marinos, V.; Vassilakis, E. 3D hazard analysis and object-based characterization of landslide motion mechanism using uav imagery. *Int. Arch. Photogramm. Remote Sens. Spat. Inf. Sci. ISPRS Arch.* **2019**, *42*, 425–430. [[CrossRef](#)]
88. Karantanellis, E.; Marinos, V.; Vassilakis, E.; Christaras, B. Object-based analysis using unmanned aerial vehicles (UAVs) for site-specific landslide assessment. *Remote Sens.* **2020**, *12*, 1711. [[CrossRef](#)]
89. Borga, M.; Gaume, E.; Creutin, J.-D.; Marchi, L. Surveying flash floods: Gauging the ungauged extremes. *Hydrol. Process.* **2008**, *22*, 3883. [[CrossRef](#)]
90. Antova, G. Application of Areal Change Detection Methods Using Point Clouds Data. *IOP Conf. Ser. Earth Environ. Sci.* **2019**, *221*, 12082. [[CrossRef](#)]
91. Ahmad Fuad, N.; Yusoff, A.R.; Ismail, Z.; Majid, Z. Comparing the performance of point cloud registration methods for landslide monitoring using mobile laser scanning data. *Int. Arch. Photogramm. Remote Sens. Spat. Inf. Sci. ISPRS Arch.* **2018**, *42*, 11–21. [[CrossRef](#)]
92. Alexiou, S.; Deligiannakis, G.; Pallikarakis, A.; Papanikolaou, I.; Psomiadis, E.; Reicherter, K. Comparing high accuracy t-lidar and uav-sfm derived point clouds for geomorphological change detection. *ISPRS Int. J. Geo-Information* **2021**, *10*, 367. [[CrossRef](#)]
93. Woodget, A.S.; Carbonneau, P.E.; Visser, F.; Maddock, I.P. Quantifying submerged fluvial topography using hyperspatial resolution UAS imagery and structure from motion photogrammetry. *Earth Surf. Process. Landforms* **2015**, *40*, 47–64. [[CrossRef](#)]
94. Niethammer, U.; James, M.R.; Rothmund, S.; Travelletti, J.; Joswig, M. UAV-based remote sensing of the Super-Sauze landslide: Evaluation and results. *Eng. Geol.* **2012**, *128*, 2–11. [[CrossRef](#)]
95. Liu, C.-C.; Chen, P.-L.; Matsuo, T.; Chen, C.-Y. Rapidly responding to landslides and debris flow events using a low-cost unmanned aerial vehicle. *J. Appl. Remote Sens.* **2015**, *9*, 096016. [[CrossRef](#)]

Disclaimer/Publisher's Note: The statements, opinions and data contained in all publications are solely those of the individual author(s) and contributor(s) and not of MDPI and/or the editor(s). MDPI and/or the editor(s) disclaim responsibility for any injury to people or property resulting from any ideas, methods, instructions or products referred to in the content.